

Gate tunable lateral 2D pn junctions: an analytical study of its electrostatics

Ferney A. Chaves, Anibal Pacheco-Sanchez, David Jiménez

Abstract

The electrostatics of two-dimensional (2D) lateral pn homojunctions considering the impact of electrostatic doping by means of two split bottom-gates are studied here. Analytical expressions are obtained from the solution of the 2D Poisson equation considering a depletion approximation. Straightforward analytical models for the electrostatic potential and the depletion width within both the dielectric and the 2D semiconductor are obtained for both the symmetrical and asymmetrical cases. In contrast to the case of devices with chemical doping, the obtained depletion width model of devices with electrostatic doping do not depend on the dielectric constant but only on the electrostatic potential and oxide thickness. The models describe the electrostatics of gate-tunable 2D pn junctions at arbitrary bias. A benchmark against numerical device simulations of MoS₂-based pn junctions validate the analytical models.

Index Terms

2D pn junction, electrostatic potential, depletion width

I. INTRODUCTION

Two-dimensional (2D) based devices have been in the spotlight of the continuous downscaling trend of electronics due to their semiconductor thin-body, high-performance and integration feasibility into standard production lines [1]. 2D pn junctions are among the most versatile emerging devices for both electronics and optoelectronics applications [2]. Homojunctions and heterojunctions have been demonstrated with 2D materials with various levels of reproducibility depending on the fabrication approach [2], [3]. In contrast to chemical doping, electrostatic doping by a pair of bottom-gate contacts separated by a gap has been demonstrated to be a more straightforward solution in controlling the different carrier concentration regions in 2D lateral (L) PN junctions. Proof-of-concept devices based on these gate tunable (GT) 2D lateral pn junctions have been experimentally proven to be suitable for optoelectronics [4]-[10], electronics [11] and neuromorphic applications [11], [12].

Modeling approaches have been presented elsewhere [13]-[16] for chemically doped 2D pn junctions, however, descriptions of the internal physical phenomena in GT 2D junctions are scarce due to the few theoretical studies on this structure [17]. In contrast to three-dimensional PN junctions where only a one-dimensional (1D) Poisson equation and the complete-depletion approximation are considered, electrostatics analysis in 2D junctions involves solving a 2D Poisson equation and the consideration of partial depletion in the transition between the depletion and quasi-neutral regions due to a weaker screening of the electric field [14], [16]. Numerical device simulations and semi-analytical solutions have been proposed for GT junctions previously for the specific case of symmetrical gate voltages [17].

In this work, a general analysis of the electrostatics of GT lateral 2D pn homojunctions, embracing both symmetric and asymmetric gate voltage tuning, yields a compact analytical model for the electrostatic potential at any location of the device cross-section. This work is organized as follows. The analytical models for the electrostatic potential and depletion width of the device under study are presented in section II. In section III, the models are applied to MoS₂ lateral pn junctions under different bias and with different device geometry and the results are discussed benchmarked with the output of an in-house numerical device simulation (NDS) tool [17]. A conclusion is provided in section IV followed by three useful appendix with details on the procedures to solve and evaluate equations in the main text.

II. DEVICE ELECTROSTATICS

The electrostatics of a GT 2D junction depicted in Fig. 1(a) can be made analytically treatable under the depletion approximation. Specifically, the electrostatic potential in the depletion region of the 2D semiconductor without chemical doping, as the one considered here, comes from the solution of the 2D Poisson equation under the assumption that there is no mobile charge inside. Fig. 1(b) shows a sketch of such a region with the boundary conditions assumed in this work. Outside of the depletion region, the electrostatic potential at each side of the pn junction, far away from the depletion region, is considered a constant and equal to the lowest and highest of the potential inside of the depletion region, those extreme values reached at the p - and n -boundary of the quasi neutral region, respectively. For this study, the physical gap between bottom-gates, l_{gap} , has been considered to be much shorter than the depletion width W_d and hence, it has been neglected. The latter consideration has no impact on the results here as discussed below (cf. section III) and shown elsewhere [17]. The device width along the

This work has received funding from the European Union's Horizon 2020 research and innovation programme under grant agreement No GrapheneCore3 881603, from Ministerio de Ciencia, Innovación y Universidades under grant agreements RTI2018-097876-B-C21(MCIU/AEI/FEDER, UE) and FJC2020-046213-I. This article has been partially funded by the European Union Regional Development Fund within the framework of the ERDF Operational Program of Catalonia 2014-2020 with the support of the Departament de Recerca i Universitat, with a grant of 50% of total cost eligible. GraphCAT project reference: 001-P-001702. We also acknowledge financial support by Spanish government under the project PID2021-127840NB-I00 (MCIN/AEI/FEDER, UE). The authors are with the Departament d'Enginyeria Electrònica, Escola d'Enginyeria, Universitat Autònoma de Barcelona, Bellaterra 08193, Spain, e-mails: FerneyAlveiro.Chaves@uab.cat, AnibalUriel.Pacheco@uab.cat, David.Jimenez@uab.cat

y -axis is large enough to consider that the junction is uniform in that direction. Thus, models presented here do not depend on the device width. Furthermore, an infinitesimally thin semiconductor considered here reduces the 2D Poisson equation to the Laplace's equation within the total computing region constrained by the following general boundary conditions: homogeneous Neumann boundary conditions at $x = 0$ and $x = W_d$ forcing a zero electric field outside the depletion region; Dirichlet boundary conditions $\phi = \phi_g(x)$ at the bottom-gate contacts ($z = 0$) whereas a non-homogeneous Neumann condition $\phi_z = \sigma(\phi)/\epsilon_{ox}$ has been set at the semiconductor plane ($z = t_{ox}$), where $\sigma = q(p - n)$ is the charge density of the 2D semiconductor with $p(n)$ as the hole(electron) carrier density, and ϵ_{ox} the dielectric permittivity. Notice that σ within the depletion region is zero for the 2D semiconductor without chemical doping as the one considered here.

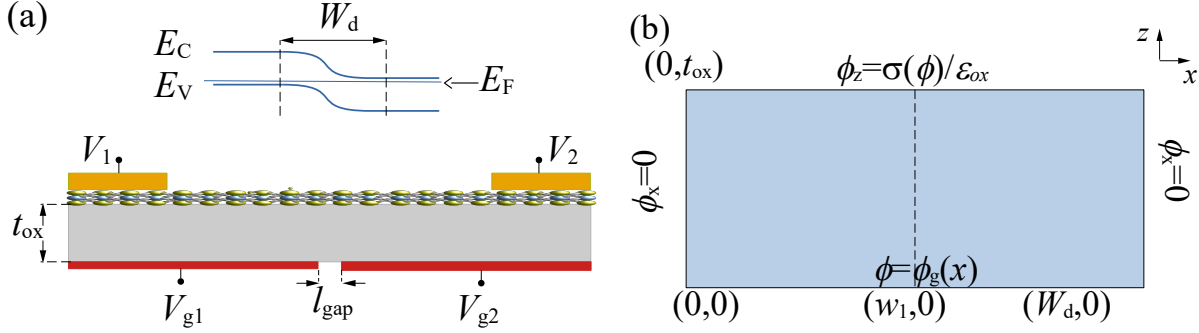


Fig. 1. (a) Bottom: schematic cross section of a gate tunable 2D pn -junction (not drawn to scale). Top: sketch of the device band diagram showing the depletion width. (b) Sketch of a symmetric depletion region showing critical coordinates and the boundary conditions required for solving the Poisson's equation within it, where $\phi_{x,z} = \partial\phi/\partial x, z$. For an asymmetric depletion region, w_1 is not the middle point in the x -direction.

The electrostatic potential profile $\phi(x, z)$, obtained from the solution of the 2D Poisson's equation within the computing region (cf. Fig.1(b)), can be expressed as (see Appendix A for details on the solving process)

$$\phi(x, z) = \sum_{k=1}^{\infty} \{A_k \cos(\lambda_k x) \cosh[\lambda_k(t_{ox} - z)]\}, \quad (1)$$

where

$$A_k = \frac{2}{\lambda_k W_d} \frac{\sin(\lambda_k w_1) (\phi_1 - \phi_2)}{\cosh(\lambda_k t_{ox})}, \quad (2)$$

with $k = 1, 2, 3, \dots$, $\lambda_k = (k\pi)/W_d$, t_{ox} the oxide thickness, w_1 the splitting point between the two gates where the electrostatic potential changes from $\phi_1 = V_{g1}$ in the gate 1 to $\phi_2 = V_{g2}$ in the gate 2. It can be inferred that for a symmetric electrostatic doping ($V_{g1} = -V_{g2}$), $w_1 = W_d/2$.

Eqs. (1) and (2) provide a general solution of the electrostatic potential of GT 2D junctions for both symmetrical ($\phi_1 = -\phi_2$) and asymmetrical ($\phi_1 \neq -\phi_2$) electrostatic doping, provided that the depletion region parameters, namely, W_d and w_1 , could be previously obtained. The latter parameters are obtained by considering the following: (i) the electrostatic potential is known at a quasi-neutral region along the 2D semiconductor, $\phi_{o1} = \phi(0, t_{ox})$, calculated at either the p - or n -type region (e.g., p -type), and (ii) that $\phi_1(0, 0) = V_{g1}$.

For (i), an analysis of the 1D electrostatics in the z -direction is required. $\phi_{o1(o2)}$ can be estimated from an analytical solution of a 1D metal-oxide-semiconductor (MOS) model obtained by considering the band profile shown in Fig. 2 and analyzed in detail in Appendix B.

The 1D MOS model [17] results in a non-linear equation for ϕ_o (cf. Eq. (B.2)), whose solution can be expressed by analytical piecewise functions. By considering an overdrive gate voltage V'_g embracing flat-band conditions (see definition in Appendix B), for a $V'_g \lesssim V_{th}$,

$$\phi_{o<} = V'_g, \quad (3)$$

and

$$\phi_{o>} = \frac{E_g}{2q} + \frac{kT}{q} \log \left\{ \exp \left[\frac{(V'_g - V_{th}) C_{ox}}{q n_0} \right] - 1 \right\}, \quad (4)$$

for $V'_g > V_{th}$, with the 2D semiconductor bandgap E_g , the Boltzmann constant k , the absolute temperature T , the electric charge q , the oxide capacitance C_{ox} , $n_0 = g_{2D} kT$ with the band-edge density of states g_{2D} (see definition in Appendix B) and the threshold voltage V_{th} defined as the 60% of $E_g/(2q)$ [17]. In order to obtain a smooth and continuous analytical function for any gate voltage, an educated solution combining Eqs. (3) and (4) yields

$$\phi_o = \phi_m - \sqrt{\phi_m^2 - \phi_{o>} \phi_{o<}}, \quad (5)$$

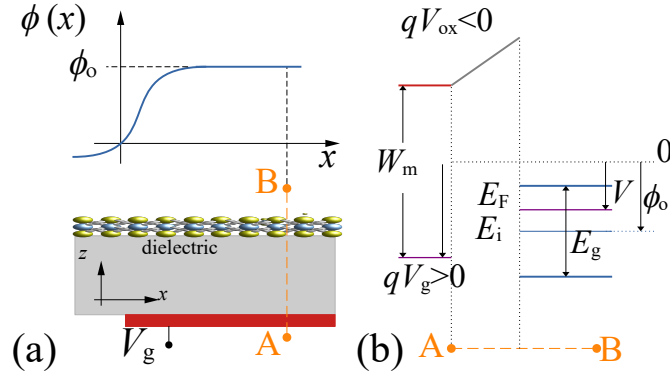


Fig. 2. (a) Bottom: a cross-section of the GT 2D pn -junction showing only one gate. Top: sketch of the electrostatic potential profile over the x -direction along the semiconductor. (b) Band profile of the metal-oxide-semiconductor structure considering the layers across the cut AB shown in the bottom part of (a).

where

$$\phi_m = \frac{1}{2}(\phi_{o>} + \mu\phi_{o<}), \quad (6)$$

with μ as a fitting parameter. As shown in Fig. 3, the proposed analytical solution matches with the numerical device simulations of the 1D MOS model considering MoS_2 as the 2D semiconductor.

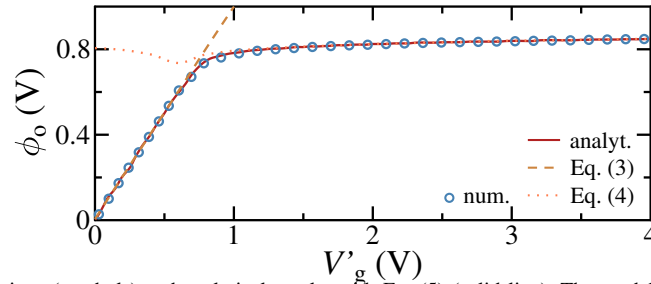


Fig. 3. ϕ_0 versus V'_g : numerical simulations (symbols) and analytical results with Eq. (5) (solid line). The model parameters are $E_g = 1.8$ eV, $t_{ox} = 300$ nm, $\epsilon_{ox} = 3.9\epsilon_0$ and $\mu = 1.003$.

By applying the conditions (i) and (ii) into Eq. (1), it is found that

$$\phi_{o1} = \sum_{k=1}^{\infty} \left[\frac{2}{\pi k} \frac{\sin\left(\pi k \frac{w_1}{W_d}\right) (\phi_1 - \phi_2)}{\cosh\left(\pi k \frac{t_{ox}}{W_d}\right)} \right], \quad (7)$$

and

$$\phi_1 = \sum_{k=1}^{\infty} \left[\frac{2}{\pi k} \sin\left(\pi k \frac{w_1}{W_d}\right) (\phi_1 - \phi_2) \right], \quad (8)$$

which are non-linear equations for the variables W_d and w_1 .

From Eq. (8) and by considering the convergence of the series $\sum_{k=1}^{\infty} [(1/(\pi k)) \sin(\pi k x)] \rightarrow (-1/2)(x-1) \forall x < 1$, the following ratio is obtained

$$\frac{w_1}{W_d} = 1 - \frac{\phi_1}{\phi_1 - \phi_2}, \quad (9)$$

from which it can be seen that for the symmetric case, i.e., $\phi_1 = -\phi_2$, $w_1 = W_d/2$ holds. By replacing Eq. (9) in Eq. (7), the following equation results

$$-\frac{1}{2} \frac{\phi_{o1}}{\phi_2} = \sum_{k=1}^{\infty} \left[\frac{1}{\pi k r} \frac{\sin(\pi k r)}{\cosh\left(\pi k \frac{t_{ox}}{W_d}\right)} \right], \quad (10)$$

with $r = \phi_2/(\phi_2 - \phi_1)$. Eq. (10) can be solved numerically to obtain W_d and, consequently, w_1 from Eq. (9).

Alternatively, a general analytical solution to obtain W_d is proposed in this work by considering the first term ($k = 1$) of the sum in Eq. (10), which leads to

$$W_d = \frac{\pi t_{\text{ox}}}{\text{sech}^{-1} \left[\frac{1}{2 \text{sinc}(r)} \frac{\phi_{\text{o1}}}{\phi_2} \right]}, \quad (11)$$

being $\text{sinc}(r)$ the normalized sinc function. Eq. (11) is valid for all values of r between 0 and 1 as long as $t_{\text{ox}}/W_d \geq 0.3$ (cf. Appendix C).

For the case of a GT 2D junction with symmetrical applied gate voltages, the depletion width is symmetrical. Hence, after some algebra, an expression for the depletion width for this case ($r = 1/2$) obtained from Eq. (10) reads

$$W_d = \frac{\pi t_{\text{ox}}}{\text{sech}^{-1} \left(-\frac{\pi}{4} \frac{\phi_{\text{o1}}}{\phi_2} \right)} \Big|_{\phi_1 = -\phi_2}, \quad (12)$$

where in contrast to a model for chemically doped 2D pn -junctions suggested elsewhere [13], [15], [16] there is no dependence on the oxide dielectric constant but only on its thickness. A phenomenological expression previously presented in [17] for W_d of 2D junctions in this same scenario, is a particular case of the general analytical solution presented here (cf. Eq. (12)). The physics-based and straightforward W_d expressions obtained here can be used also to calculate transport-related parameters of 2D junctions [18], [19], however, this is out of the scope of the present study.

III. RESULTS AND DISCUSSION

The model presented here has been evaluated considering a $2\mu\text{m}$ -long MoS_2 lateral pn -junction. Unless stated otherwise, a 300nm -thick SiO_2 oxide separates the back-gates and the 2D semiconductor. I_{gap} is considered 0 as in the analytical model. Furthermore, previous studies have shown that I_{gap} defines mostly W_d by a linear relation for long enough values [17]. The device has been studied in two different scenarios: with symmetric ($V_{g1} = -V_{g2}$) and asymmetric ($V_{g1} \neq -V_{g2}$) electrostatic doping. Hereinafter, V_{gx} indicates the overdrive gate voltage unless stated otherwise. Numerical device simulations (NDS) have been performed to benchmark the analytical approach presented here (cfs. Figs. 4-5). W_d in the NDS tool corresponds to the semiconductor V_g -induced charge $Q_{\text{sc}}(x)$ is equal to 43.6% of the induced charge at each side of induced charge regions of the junction. Further details on the experimentally-calibrated in-house physics-based simulation tool can be found elsewhere [17]. In Fig. 4 and Fig. 5 both the 2D electrostatic potential inside the dielectric and the 1D electrostatic potential in the semiconductor for the symmetric and asymmetric cases are shown, respectively. Fig. 6 shows the depletion width dependence on the gate voltages for some symmetric and asymmetric cases with different values of t_{ox} .

For the symmetric case, gate voltages of $\pm 1.5\text{V}$ and $\pm 10\text{V}$ have been used, yielding $r = 1/2$ for each electrostatic doping. The symmetric electrostatic potential (cf. Eq. (1)) has been obtained with the model within the device depletion region for both inside the oxide and at the 2D semiconductor, provided $W_d (\approx 0.6\mu\text{m})$ has been calculated with Eq. (12), as shown in Figs. 4(a) for $V_{g1} = -V_{g2} = -1.5\text{V}$, and (b) for both gate voltages, respectively.

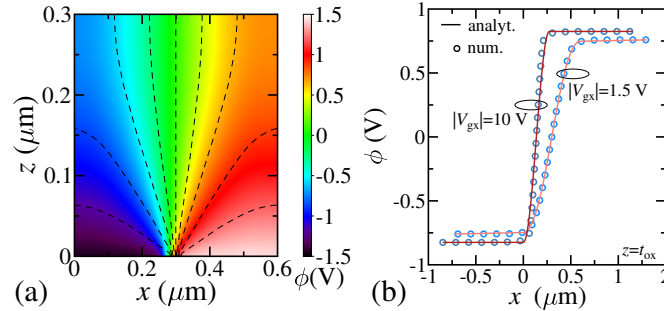


Fig. 4. Electrostatic potential of a 2D MoS_2 junction with symmetrical applied voltages. (a) Analytical results within the depletion region inside the oxide obtained with Eq. (1) for $V_{g1} = -V_{g2} = -1.5\text{V}$. Dashed lines are the equipotential lines. (b) Analytical (lines) and numerical simulation results (symbols) along the $2\mu\text{m}$ 2D semiconductor for $V_{g1} = -V_{g2} = -1.5\text{V}$ and -10V .

The equipotential line at $x = w_1 \approx 0.3\mu\text{m}$ in Fig. 4(a) corresponds to $\phi = 0$. The symmetric distribution of the total electrostatic potential within the oxide can be observed along the x -direction, i.e., $\phi(0 \leq x \leq w_1, z) = -\phi(w_1 \leq x \leq W_d, z)$. Interestingly, the electric field lines¹ in gate tunable lateral 2D pn -junctions here studied are different to those generated in chemically doped lateral 2D pn -junctions, as studied in refs. [14]-[16] where there is a non-zero component of the electric field perpendicular to the semiconductor plane inside the dielectric next to the semiconductor in the depletion region. However, for GT devices, such electric field component is vanished, and hence, there is a very weak dependence of W_d (Eq. (11)) on ϵ_{ox} in contrast with the chemical doped case.

The analytical model successfully describes the symmetric electrostatic potential profile along the 2D semiconductor (at $z = t_{\text{ox}}$) as shown in Fig. 4(b) by comparing it with numerical simulation results of the same device at different bias. These curves exhibit depletion widths of $\sim 0.6\mu\text{m}$ and $0.27\mu\text{m}$ for $V_{g1} = -V_{g2} = -1.5\text{V}$ and $V_{g1} = -V_{g2} = -10\text{V}$, respectively, which correspond to the calculated values by means of Eq. (12) with $\phi_{\text{o1}} = -0.75\text{V}$ and -0.82V from Eq. (5). The left ($x < 0$) in the

¹Electric field lines are perpendicular to the equipotential lines.

computational region) and right ($x > W_D$) 2D semiconductor quasi-neutral regions are described by the minimum and maximum values of ϕ (obtained with the analytical approach used here, cf. Eq. (5)), respectively, in the corresponding depletion region.

For the asymmetric case, the same MoS₂-based *pn* junction studied above ($t_{\text{ox}} = 300\text{nm}$) has been biased at three different configurations. Fig. 5(a) shows the potential contour plot with equipotential lines from the analytical model for the case with $V_{g1} = -20\text{V}$ and $V_{g2} = 10\text{V}$ ($r = 0.33$) exhibiting $W_d \approx 0.23\mu\text{m}$ and $w_1 \approx 0.09\mu\text{m}$, as given by Eq. (9). The different electrostatic doping induced by each gate breaks the symmetry of ϕ within the computational region as observed by the analytical modeling (cf. Eq.(1)). A zero perpendicular electric field component next to the semiconductor can be observed, similar to the symmetric case, explaining the weak dependence of W_d on ϵ_{ox} even in the asymmetric case.

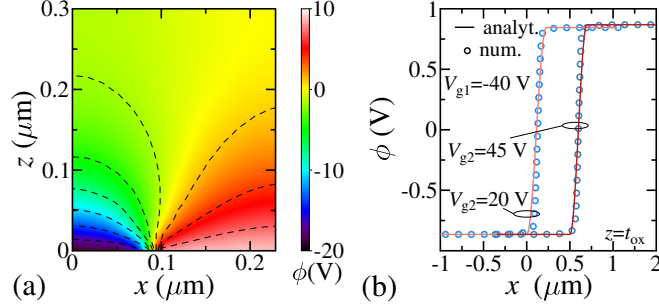


Fig. 5. Electrostatic potential of a 2D MoS₂ junction with asymmetrical applied voltages ($V_{g1} \neq -V_{g2}$). (a) Analytical results within the computational region obtained with Eq. (1) at $V_{g1} = -20\text{V}$ and $V_{g2} = 10\text{V}$. (b) Analytical (lines) and numerical simulation results (symbols) along the 2D semiconductor at different gate voltages. Electrostatic potentials for the case with smallest asymmetry have been shifted to the right by an amount of $0.5\mu\text{m}$ for visualization purposes.

Fig. 5(b) shows analytical and numerical results of the electrostatic potential along the 2D semiconductor of GT MoS₂ junction at two different asymmetric bias sets: $V_{g1} = -40\text{V}$; $V_{g2} = 20\text{V}$ (strong asymmetry $r = 0.33$) and for $V_{g1} = -40\text{V}$; $V_{g2} = 45\text{V}$ (small asymmetry $r = 0.53$) exhibiting predicted W_d equal to $\sim 0.23\mu\text{m}$ and $\sim 0.20\mu\text{m}$, respectively. The more asymmetric the electrostatic doping is the more distant is w_1 from $W_d/2$. Hence, $\phi(x - w_1 = 0, t_{\text{ox}}) \neq 0\text{V}$ in contrast to the symmetric scenario.

The analytical depletion width model (cf. Eqs. (11) and (12)) is able to describe NDS results of both symmetric and asymmetric GT MoS₂ junctions with different t_{ox} . Fig. 6(a) shows the analytical (cf. Eq. (12)) and NDS results of W_d for symmetric *pn*-junctions as a function of ϕ_{o1}/ϕ_2 . As example cases, the ratio takes values of 0.5 and 0.082 for the two symmetrical devices described in Fig. 4(b).

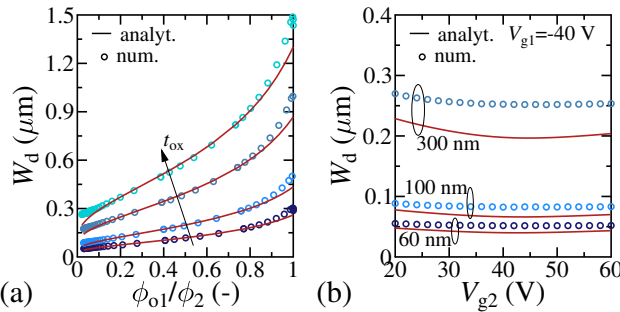


Fig. 6. Variation of the depletion width of (a) symmetric GT 2D junction with the ratio ϕ_{o1}/ϕ_2 for t_{ox} equal to 60 nm, 100 nm, 200 nm and 300 nm, and of (b) asymmetric GT 2D junction with V_{g2} for 3 different t_{ox} . Symbols are numerical device simulation results and lines are results from the analytical model proposed here.

The depletion widths obtained with the analytical model (cf. Eq. (11)) for asymmetric GT MoS₂ junctions with different t_{ox} are compared to NDS results in Fig. 6(b). The electrostatic doping is enabled by applying $V_{g1} = -40\text{V}$ and sweeping V_{g2} from 20 V to 60 V, yielding a minimum and maximum values of r equal to 0.3 and 0.6, respectively. The V_{g2} -dependence of W_d at different t_{ox} is qualitatively captured by the model. The maximum relative error for the analytical results in comparison to the NDSs is of $\sim 21\%$ for the devices under study. The origin of this deviation is discussed next.

W_d values from NDS could, in fact, be lower than the ones reported here in the asymmetric case due to the not unique definition of the computational space related to depletion region, specially its beginning and ending, i.e., the x -limits. In this work, we have assumed the same criterium of the 43.6% of the induced charge density in the quasi-neutral regions like in the symmetric case [16], [17]. However, due to the large transition region separating the fully depletion region and the quasi-neutral depletions regions exhibited by 2D lateral *pn*-junctions in comparison to 3D *pn*-junctions, as discussed elsewhere [16], this criterium could be relaxed for devices with asymmetric electrostatic doping and pristine 2D semiconductors towards an improved description of the NDS by the analytical model. Additionally, the 1D analytical model of $\phi_{o1(o2)}$ might be another source of error since it only considers the impact of one gate voltage in contrast to the 2D numerical solution depending on both applied bias. By considering these discussions and by showing that all conditions are fulfilled, i.e., $0 < r < 1$ and $t_{\text{ox}}/W_d > 0.3$, the analytical model of W_d in the asymmetric scenario, can be used to set reliable minimum limit of values.

IV. CONCLUSION

The 2D Poisson equation has been solved analytically yielding models for the electrostatic potential and depletion width of GT 2D lateral *pn*-junctions with symmetric and asymmetric electrostatic doping applied by two separated bottom-gates. The analytical ϕ model enables to elucidate the electrostatic potential within both the oxide and the 2D semiconductor, regardless the symmetric bias conditions. The analytical ϕ and W_d models have been benchmarked against numerical device simulations of GT MoS₂-based junctions. For the symmetric electrostatic doping scenario ($V_{g1} = -V_{g2}$), the physics-based analytical model is able to describe the NDS results within the 2D semiconductor at all bias and for different oxide thickness; whereas for the asymmetric scenario ($V_{g1} \neq -V_{g2}$), the model captures the bias dependence of practical cases for different oxide thicknesses while yielding reliable W_d minimum values within a confidence range of $\gtrsim 80\%$. The straightforward analytical models proposed here for the electrostatics of GT 2D junctions intend to be of aid for technology improvements by unveiling some aspects of the internal physical mechanisms as well as for the modeling community by considering the expressions provided here in electrostatics-dependent transport models.

APPENDIX A. SOLUTION OF THE 2D POISSON EQUATION

The electrostatic potential within the depletion region can be expressed as the product of an x -dependent function $X(x)$ and a z -dependent function $Z(z)$, i.e., $\phi(x, z) = XZ$. Hence, by separation of variables, the Laplace's equation ($\nabla^2\phi = 0$) reads

$$Z \frac{\partial^2 X}{\partial x^2} + X \frac{\partial^2 Z}{\partial z^2} = 0, \quad (\text{A.1})$$

from which a differential partial equation system can be obtained by dividing Eq. (A.1) by XZ such as

$$\frac{\partial^2 X}{\partial x^2} + \lambda^2 X = 0, \quad (\text{A.2a})$$

$$\frac{\partial^2 Z}{\partial z^2} - \lambda^2 Z = 0, \quad (\text{A.2b})$$

with

$$\lambda^2 = -\frac{1}{X} \frac{\partial^2 X}{\partial x^2} = \frac{1}{Z} \frac{\partial^2 Z}{\partial z^2}. \quad (\text{A.3})$$

The solutions of Eq. (A.2) can be expressed in a general form as

$$X(x) = a_k \sin(\lambda_k x) + b_k \cos(\lambda_k x), \quad (\text{A.4a})$$

$$Z(z) = c_k \exp(-\lambda_k z) + d_k \exp(\lambda_k z), \quad (\text{A.4b})$$

for $\lambda^2 > 0$ and

$$X(x) = a_k \exp(-\lambda_k x) + b_k \exp(\lambda_k x), \quad (\text{A.5a})$$

$$Z(z) = c_k \sin(\lambda_k z) + d_k \cos(\lambda_k z), \quad (\text{A.5b})$$

for $\lambda^2 < 0$. In this work, the former case ($\lambda^2 > 0$) has been considered without loss of generality.

By using Eq. (A.4a) and the Neumann boundary conditions $\phi_x(x=0) = 0$ and $\phi_x(x=W_d) = 0$ (cf. Fig. 1(b)) lead to find $a_k = 0$ from the former boundary condition and consequently, $\sin(\lambda_k W_d) = 0$ for the second one, from which the $\lambda = k\pi/W_d$ is obtained where $k = 1, 2, 3, \dots$. Therefore,

$$X(x) = b_k \cos\left(\frac{k\pi}{W_d}x\right). \quad (\text{A.6})$$

Similarly, by considering Eq. (A.4b), the evaluation of $\phi_z = 0$ at $z = t_{ox}$ yields $c_k = d_k \exp(2\lambda_k t_{ox})$, leading to

$$Z(z) = 2d_k \exp(\lambda_k t_{ox}) \cosh[\lambda_k(t_{ox} - z)]. \quad (\text{A.7})$$

By using Eqs. (A.6) and (A.7) in the proposed definition of the electrostatic potential, Eq. (1) is found, whereas the definition of A_k is obtained as follows.

The value of the electrostatic potential at $z = 0$ along the x -direction $\phi(x, 0) = \phi_g(x)$ reads as

$$\phi_g(x) = \sum_{k=1}^{\infty} [A_k \cos(\lambda_k x) \cosh(\lambda_k t_{ox})]. \quad (\text{A.8})$$

Solving Eq. (A.8) for A_k leads to

$$A_k = \frac{\int_0^{W_d} \phi_g(x) \cos(\lambda_k x) dx}{\cosh(\lambda_k t_{ox}) \int_0^{W_d} \cos^2(\lambda_k x) dx}. \quad (\text{A.9})$$

The integral in the denominator yields $W_d/2$. Since $\phi_g(x) = \phi_1$ for $x < w_1$ and $\phi_g(x) = \phi_2$ for $x > w_1$, the integral in the numerator can be split in a sum of integrals such as $\int_0^{W_d} = \int_0^{w_1} + \int_{w_1}^{W_d}$. Hence,

$$\int_0^{w_1} \phi_1 \cos(\lambda_k x) dx = \frac{\phi_1}{\lambda_k} \sin(\lambda_k w_1), \quad (\text{A.10a})$$

$$\int_{w_1}^{W_d} \phi_2 \cos(\lambda_k x) dx = -\frac{\phi_2}{\lambda_k} \sin(\lambda_k w_1). \quad (\text{A.10b})$$

Eq. (2) is hence determined by substituting the solutions of the integrals in Eq. (A.9).

APPENDIX B. 1D MOS MODEL

The band profile of a transversal 1D section of the GT 2D pn -junction (Fig. 2(a)) is shown in Fig. 2(b). The section is chosen in a way that the Fermi level energy E_F considered is far away from the depletion region. From this band profile and by considering the charge conservation law, i.e., $Q_m + Q_{sc} = 0$, and the voltage Kirchoff's law, i.e., $W_m - qV_{ox} = \chi + E_g/2 - q\phi_o + qV_g$, the following relation can be obtained

$$[\chi + E_g/2 - q\phi_o + qV_g - W_m] \frac{C_{ox}}{q} + Q_{sc}(\phi_o - V) = 0 \quad (\text{B.1})$$

with the semiconductor electron affinity χ , the band gap of the 2D semiconductor E_g , the metal work function W_m , the gate charge density Q_m and the V_g -induced carrier charge density $Q_{sc}(= \sigma)$ in the semiconductor which is a function of the local electrostatic potential ϕ_o and of an electrochemical potential V (arbitrarily referred).

In order to calculate ϕ_o , for instance in the n -region and assuming thermal equilibrium with $V = 0$, $Q_{sc} \approx -qn = -qn_0 \log \{1 + \exp[(q\phi_o - E_g/2)/(kT)]\}$, where $n_0 = g_{2D}kT = [g_v g_s m / (2\pi h^2)] kT$ defined by the band-edge effective mass, spin and valley degeneracy factors m , g_v , g_s of the 2D semiconductor, respectively. Therefore, Eq. (B.1) can be written as

$$(-\phi_o + V'_g) C_{ox} - qn_0 \log \{1 + \exp[(q\phi_o - E_g/2)/(kT)]\} = 0, \quad (\text{B.2})$$

which is a transcendental equation for ϕ_o with $qV'_g = qV_g - W_m + \chi + E_g/2$, where the term $W_g - \chi - E_g/2$ describes the flat-band voltage. A piecewise analytical solution for Eq. (B.2) is given by Eqs. (3)-(5) in the main text. The model works regardless the device geometry and dielectric properties since in the hypothetical worst case where $C_{ox} = -qn_0/(V'_g - V_{th})$, i.e., $\phi_o > = E_g/(2q)$ (cf. Eq. (4)), a solution still exists for Eq. (5).

For the analytical results presented in this work, the following parameter values have been considered: $T = 300\text{K}$, $g_v = g_s = 2$, $E_g = 1.8\text{eV}$ and $m = 0.57m_0$ where m_0 is the free electron mass. The same values have been used in the numerical device simulations in [17].

APPENDIX C: VALIDITY OF CONDITIONS FOR THE ANALYTICAL W_d MODEL

Fig. 7 shows results of Eq. (10) as a function of $\xi = t_{ox}/W_d$ with k -terms. For the symmetric case (Fig. 7(a)), ϕ_{o1} depends on $V_{g1} = V_{g2}$ whereas, for the asymmetric case (Fig. 7(b)), ϕ_{o1} is constant since V_{g1} is fixed and V_{g2} varies.

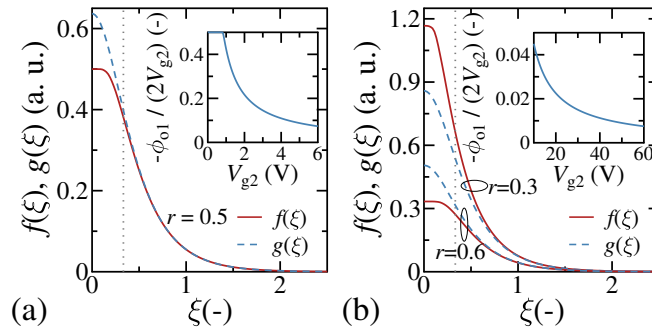


Fig. 7. Right side of Eq. (10) calculated with one ($k=1$) and several terms (k from 1 to 1200) terms for (a) symmetric and (b) asymmetric electrostatic doping. Insets: results of the left side of Eq. (10). Dotted line indicates $\xi = 0.3$ and is added as a guide for the eye. Values considered for this study are $t_{ox} = 300\text{nm}$ for all cases whereas ϕ_{o1} is equal to 0.89 for the asymmetric case.

$f(\xi)$ and $g(\xi)$ correspond to the summatory on the right side of Eq. (10) calculated with one ($k=1$) and several terms (k from 1 to 1200), respectively. It is observed that $g(\xi) \approx f(\xi)$ for $\xi > 0.3$ for the symmetric (Fig. 7(a)) and asymmetric cases (Fig. 7(b)). The left side of Eq. (10) (cf. insets of Fig. 7) has values below 0.4 and 0.03 in the symmetric and asymmetric scenarios for the gate voltages used in each case. The latter indicates also that $g(\xi) \approx f(\xi)$ holds for all the devices and cases under study.

These results validate Eq. (11) as equivalent to Eq. (10).

REFERENCES

- [1] D. Akinwande, C. Huyghebaert, C.-H. Wang, M. I. Serna, S. Goossens, L.-J. Li, H.-S. Philip Wong, F. H. L. Koppens, "Graphene and two-dimensional materials for silicon technology", *Nature*, vol. 573, pp. 507–518, 2019. DOI: 10.1038/s41586-019-1573-9
- [2] F. Wang, K. Pei, Y. Li, H. Li, T. Zhai, "2D Homo Junctions for Electronics and Optoelectronics", *Advanced Materials*, vol. 33, 2005303, Apr. 2021. DOI: 10.1002/adma.202005303
- [3] Y. Liu, Y. Huang, X. Duan, "Van der Waals integration before and beyond two-dimensional materials", *Nature*, vol. 567, pp. 323–333, Mar. 2019. DOI: 10.1038/s41586-019-1013-x
- [4] A. Pospischi, M. M. Furchi, T. Mueller, "Solar-energy conversion and light emission in an atomic monolayer p–n diode", *Nature Nanotechnology*, vol. 9, pp. 257–261, Mar. 2014. DOI: 10.1038/nnano.2014.14
- [5] B. W. H. Baugher, H. O. H. Churchill, Y. Yang, P. Jarillo-Herrero, "Optoelectronic devices based on electrically tunable p–n diodes in a monolayer dichalcogenide", *Nature Nanotechnology*, vol. 9, pp. 262–267, Mar. 2014. DOI: 10.1038/nnano.2014.25
- [6] J. S. Ross, P. Klement, A. M. Jones, N. J. Ghimire, J. Yan, D. G. Mandrus, T. Taniguchi, K. Watanabe, K. Kitamura, W. Yao, D. H. Cobden, X. Xu, "Electrically tunable excitonic light-emitting diodes based on monolayer WSe₂ p–n junctions", *Nature Nanotechnology*, vol. 9, pp. 268–272, Mar. 2014. DOI: 10.1038/nnano.2014.26
- [7] M. Buscema, D. J. Groenendijk, G. A. Steele, H. S.J. van der Zant, A. Castellanos-Gomez, "Photovoltaic effect in few-layer black phosphorus PN junctions defined by local electrostatic gating", *Nature Communications*, vol. 5, Article number : 4651, Aug. 2014. DOI: 10.1038/ncomms5651
- [8] S. Memaran, N. R. Pradhan, Z. Lu, D. Rhodes, J. Ludwig, Q. Zhou, O. Ogunsolu, P. M. Ajayan, D. Smirnov, A. I. Fernandez-Dominguez, F. J. Garcia-Vidal, L. Balicas, "Pronounced Photovoltaic Response from Multilayered Transition Metal Dichalcogenides PN-Junctions", *Nano Letters*, vol. 15, pp. 7532–7538, Oct. 2015. DOI: 10.1021/acs.nanolett.5b03265
- [9] Z. Wang, F. Wang, L. Yin, Y. Huang, K. Xu, F. Wang, X. Zhan, J. He, "Electrostatically tunable lateral MoTe₂ p–n junction for use in high-performance optoelectronics", *Nanoscale*, vol. 8, no. 27, pp. 13245–13250, Jun. 2016. DOI: 10.1039/C6NR02231F
- [10] Y.-Q. Bie, G. Grosso, M. Heuck, M. M. Furchi, Y. Cao, J. Zheng, D. Bunandar, E. Navarro-Moratalla, L. Zhou, D. K. Efetov, T. Taniguchi, K. Watanabe, J. Kong, D. Englund, P. Jarillo-Herrero, "A MoTe₂-based light-emitting diode and photodetector for silicon photonic integrated circuits", *Nature Nanotechnology*, vol. 12, pp. 1124–1129, Oct. 2017. DOI: 10.1038/nnano.2017.209
- [11] C. S. Pang, C. Y. Chen, T. Ameen, S. Zhang, H. Ilatikhameneh, R. Rahman, G. Klimeck, Z. Chen, "WSe₂ Homo Junction Devices: Electrostatically Configurable as Diodes, MOSFETs, and Tunnel FETs for Reconfigurable Computing", *Small*, vol. 15, 1902770, Aug. 2019. DOI: 10.1002/sml.201902770
- [12] C. Pan, C.-Y. Wang, S.-J. Liang, Y. Wang, T. Cao, P. Wang, C. Wang, S. Wang, B. Cheng, A. Gao, E. Liu, K. Watanabe, T. Taniguchi, F. Miao, "Reconfigurable logic and neuromorphic circuits based on electrically tunable two-dimensional homo junctions", *Nature Electronics*, vol. 3, no. 7, pp. 383–390, Jun. 2020. DOI: 10.1038/s41928-020-0433-9
- [13] A. Sh. Achoyan, A. É. Yesayan, É. M. Kazaryan, S. G. Petrosyan, "Two-dimensional p–n junction under equilibrium conditions", *Semiconductors*, vol. 36, pp. 903–907, 2002. DOI: 10.1134/1.1500469
- [14] A. Nipane, S. Jayanti, A. Borah, J. T. Teheran, "Electrostatics of lateral p–n junctions in atomically thin materials", *Journal of Applied Physics*, vol. 122, 194501 Nov. 2017. DOI: 10.1063/1.4994047
- [15] H. Ilatikhameneh, T. Ameen, F. Chen, H. Sahasrabudhe, G. Klimeck, R. Rahman, "Dramatic Impact of Dimensionality on the Electrostatics of P–N Junctions and Its Sensing and Switching Applications", *IEEE Transactions on Nanotechnology*, vol. 17, no. 2, pp. 293–298, Mar. 2018. DOI: 10.1109/TNANO.2018.2799960
- [16] F. A. Chaves, D. Jiménez, "Electrostatics of two-dimensional lateral junctions", *Nanotechnology*, vol. 29, no. 27, 275203, May 2018. DOI: 10.1088/1361-6528/aabeb2
- [17] F. A. Chaves, D. Jiménez, "The gate tunable 2D pn junction driven out-of-equilibrium", *Journal of Applied Physics*, vol. 130, 174505, Nov. 2021. DOI: 10.1063/5.0063144
- [18] T. Low, S. Hong, J. Appenzeller, S. Datta, M. S. Lundstrom, "Conductance Asymmetry of Graphene p–n Junction", *IEEE Transactions on Electron Devices*, vol. 56, no. 6, pp. 1292–1299, Jun. 2009. DOI: 10.1109/TED.2009.2017646
- [19] B. Gharekhanlou, S. Khorasani, "Current–Voltage Characteristics of Graphene p–n Junctions", *IEEE Transactions on Electron Devices*, vol. 57, no. 1, pp. 209–214, Jan. 2010. DOI: 10.1109/TED.2009.2034494